Ocean Engineering 300 (2024) 117469

Contents lists available at ScienceDirect

Ocean Engineering

journal homepage: www.elsevier.com/locate/oceaneng

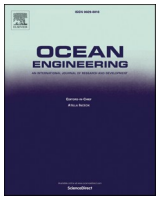

Research paper

Impact of initial slide on downslope seafloor with a weak layer

Yunrui Han [a], Wangcheng Zhang [b,**], Long Yu [a,*], Zhongtao Wang [a], Qing Yang [a]

[a] State Key Laboratory of Coastal and Offshore Engineering, Dalian University of Technology, Dalian, 116024, China
[b] Department of Engineering, Durham University Institute for Geotechnical Engineering, ETH Zurich, 8093, Zurich, Switzerland

ARTICLE INFO

Keywords:
Submarine landslides
Slide mass
Weak layer
Progressive failure
Strength

ABSTRACT

Submarine landslides are a major offshore geohazard posing increasing threat to offshore and coastal developments. A submarine landslide may usually involve multistage failure triggered by the first failure. During submarine landslide evolution, the emergent sliding mass may act as an impact load on the downslope seafloor potentially leading to surficial erosion of sediments or deeper ploughing failure with the presence of a weak layer. The study presents a comprehensive analysis of seafloor instability and post-failure behaviors subjected to the first slide mass impact, using a large deformation finite element (LDFE) method. Different failure patterns are investigated and the corresponding critical impact loads for triggering the seafloor instability are analyzed. The parameters controlling the strain softening behaviors of soils and the undrained shear strength in the weak layer have significant effects on the critical condition for the seafloor failure. The dynamic inertia of the slide mass, however, has little effect on the results. An empirical equation for assessing the seafloor instability subjected to the first slide impact, with respect to the impact load from the initial slide and the gravity stress relative to the shear strength in the weak layer, is proposed based on a parametric study.

1. Introduction

Continuing offshore exploitation of traditional hydrocarbons, such as oil and gas, as well as renewables suggest a necessity to fully understand submarine landslide geohazard. Submarine landslides are often considered as a major geohazard posing significant threats to offshore infrastructure and coastal communities (Piper et al., 1999; Randolph and White, 2012; Liu et al., 2015; Casalbore et al., 2012). Drawing from typical geological survey findings, exemplified by events like the Baiyun Slide and Brunei Slide in the South China Sea, analysis suggests that submarine landslides are also recognized as significant contributors to tsunamis (Z. Ren et al., 2019, 2023; Sun et al., 2022; Løvholt et al., 2015). The submarine landslides can occur in very gentle continental slopes and are of large scale compared to their subaerial counterparts. Their morphologies and potential causes have been considerably observed and discussed in the literature, for example for the Storegga Slide in the Norwegian Sea (Bryn et al., 2005; Bugge et al., 1988; Haflidason et al., 2005) and the Canary Slide in the West African continental margin (Krastel et al., 2001).

Progressive failure that may occur both onshore and offshore, is considered a major reason for the occurrence of enormous landslides (Bernander, 1978; Locat et al., 2011; Puzrin et al., 2017; Zhang et al., 2017), which can be hardly explained with the classical limit equilibrium method. Particularly, the translational progressive failure with shear band propagation (SBP) along a weak layer has been extensively studied during the last two decades (Dey et al., 2015, 2016b, 2016c; Puzrin et al., 2015b; Zhang et al., 2016). The weak layer is defined as an embedded soil layer where the soil shear strength relative to the overburden pressure is lower than that of adjacent layers. Recent site investigations have revealed that the existence of weak layer might be a pre-conditioning factor for progressive failure in many large-scale submarine landslides (Dan et al., 2007; Kvalstad et al., 2005; Locat et al., 2013, 2015; Sultan et al., 2010). With a certain external trigger, the shear stress in the weak layer might reach the peak shear strength followed by strength reduction with further shearing. After accumulation of a considerable amount of plastic deformation within the weak layer, catastrophic SBP might occur followed by slab failure and retrogression (Zhang et al., 2019, 2021).

Submarine landslides may originate from different external factors such as earthquakes (Puzrin et al., 2015a), toe erosion (Dey and

* Corresponding author.
** Corresponding author.
E-mail addresses: hyr2021@dlut.edu.cn (Y. Han), wangcheng.zhang@durham.ac.uk (W. Zhang), longyu@dlut.edu.cn (L. Yu), zhongtao@dlut.edu.cn (Z. Wang), qyang@dlut.edu.cn (Q. Yang).

https://doi.org/10.1016/j.oceaneng.2024.117469
Received 22 December 2023; Received in revised form 27 February 2024; Accepted 9 March 2024
Available online 18 March 2024

Hawlader, 2015; Locat and Jostad, 2013; Quinn et al., 2012), rapid sedimentation (Martorelli et al., 2016; Moernaut et al., 2017; Stoecklin et al., 2017), volcanic eruption (Casalbore et al., 2020; Watt et al., 2012) and human construction activities (Bernander et al., 2016; Dey and Hawlader, 2016b). A submarine landslide often involves multistage failure including retrogression upslope and ploughing downslope (Puzrin and Gray, 2017), after initial failure. It has been widely accepted that submarine landslides can be initiated locally, typically at the steepest point within a weak layer, and that upward retrogressive failure can expand their scale (Zhang et al., 2021). Two downslope seafloor post-failure mechanisms, i.e. frontally confined and frontally emergent, have been commonly observed in historical events (Frey-Martínez et al., 2006; Madrussani et al., 2018). The post-failure criteria and their relationships with the first failure, however, have not been fully understood. Meanwhile, during submarine landslide evolution, the emergent sliding mass may act as an impact load on the downslope seafloor potentially leading to surficial erosion of sediments or deeper failure with SBP along a weak layer. The present study focuses on the latter consequence. Landslides or avalanches triggered by sudden impact loads are not rare, e.g., snow avalanches caused by skiers and snowboarders observed in some footages. Folded basin-filling sediments observed in some historical events, e.g., the Storegga Slide (Bryn et al., 2005; Haflidason et al., 2005) and the Ritter Slide (Watt et al., 2019), may suggest subsequent failure of downslope seafloor caused by an initial smaller slide.

Given that the source area of submarine landslides, such as the Storregga slide, can encompass the region below the initiation point, reaching flat terrain, we believe that progressive downward failure by the first (initial) failure is likely the cause. The present study aims to propose a novel failure mechanism involving the subsequent failure of the downslope seafloor triggered by an initial smaller slide, providing a reference to explain the failure mechanism of ancient large-scale landslides, such as the Storegga event. Both static and dynamic models were employed to validate this proposed mechanism by using a large deformation finite element (LDFE) analysis, and introduced a method for quantitatively assessing the impact of sliding masses on seabed stability.

2. Problem definition

The whole process of a submarine landslide generally involves disintegration of failed blocks from solid to fluid, debris flow with a possible evolution to turbidity, and final deposition (Boukpeti et al., 2012; Masson et al., 2006; Rui and Yin, 2019; Zhang and Randolph, 2020), as shown in Fig. 1. With a short travelling distance from the source, the sliding mass might remain intact with shearing mainly taking place at the frictional shear surface. After entrainment of ambient water, the solid sliding mass may evolve into a debris flow, travelling for several to thousands of kilometres before re-stabilization (Boukpeti and White, 2012).

Typical characteristics, such as the maximum run-out velocities and travel distances, of some reported historical submarine landslides are summarized in Table 1. The slope angles of these historical events are usually small (1°–5°) compared with the onshore landslides, which, however, may lead to very large scale of spread failure (Hance, 2003; Masson et al., 2006). The thickness of the sliding mass is usually in a range of 2–50 m (Elverhøi et al., 1997; Kopf et al., 2016; Laberg and Vorren, 1995; Masson et al., 2006; Migeon et al., 2012), though the thickness of the Storegga slide deposit can be up to 430 m (Haflidason et al., 2004). The run-out velocity of the submarine sliding mass is estimated in a range of 0.7–60 m/s while the run-out distance can be up to thousands of kilometres (Gue, 2012; Talling, 2014). The first failure of a large submarine landslide can cover a much smaller volume, which may further trigger subsequent failures under certain conditions leading to an enormous submarine landslide complex (Longva et al., 2003). Multi-stage failure is commonly observed in submarine landslides such as the Finneidfjord Slide offshore Norway (L'Heureux et al., 2012), though its mechanism especially the downslope progressive failure has been less understood. The mechanisms of the subsequent failures are diverse depending on the role of the first failure. The release of the first failure may lead both to retrogression upslope and the ploughing or erosion of intact sediments downslope. The present study focuses on the latter process: with the impact of the upstream sliding mass or slide, the downslope seafloor collapse (representing a second failure) with SBP along the weak layer and global slab failure, as shown in Figs. 1 and 2. Here, for the second failure, the impact load from the initial slide is an external factor which suddenly alters the stress state of the downstream seafloor while the presence of the weak layer is an internal factor which determines the locus of the shear surface.

First, the sliding mass is assumed in a quasi-static state which is relevant to the steady flow phase with constant velocity or near-deposition stage with negligible velocity, such that the dynamic impact is ignored. The dynamic effect will also be simulated and discussed later in the study. Although the configuration of the sliding mass is related to the breakup, water entrainment and hydroplaning (Mohrig et al., 1998), a simplified rectangular sliding mass is considered in the present study, as shown in Fig. 2. Therefore, the simplified problem is somewhat analogy to the embankment failure caused by the sudden surcharge (Early and Skempton, 1972). The impact load of the initial slide on the seafloor comprises two components: the pressure perpendicular to the seabed surface (p) and shear stress along the seabed surface (τ) (Acosta et al., 2017; De Blasio et al., 2004; Iverson and George, 2019; Mohrig et al., 1998; Yin and Rui, 2018). The value of p is given by

$$p = \gamma' h \cos\theta \tag{1}$$

where θ denotes the seafloor inclination, h the thickness of the sliding mass, and γ' the buoyant unit weight of the sliding mass; while the shear stress is given by

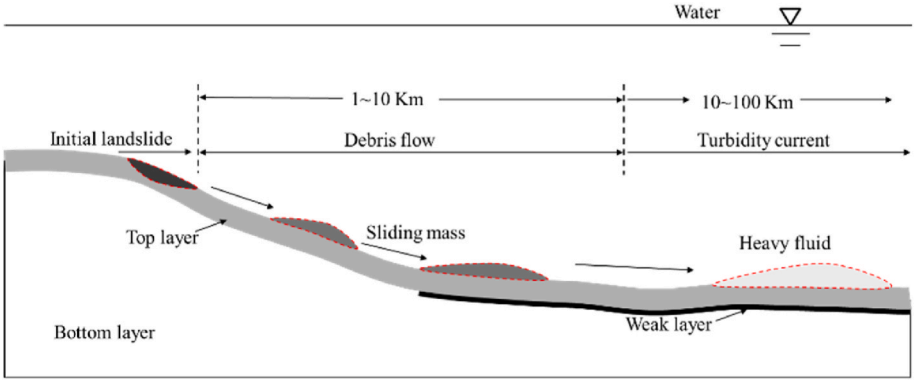

Fig. 1. Sketch showing the whole process of a submarine landslide.

Table 1
Characteristics of some typical submarine landslides.

Name of historical event	Slope angle (°)	Impacted area (km^2)	Sliding mass thickness, h (m)	Velocity, v (m/s)	Run-out distance (km)	Reference
Messina slide	3	–	20	6.0	–	Mohrig et al. (1998)
Orleansville slide	15	–	20	19.5	–	
Sandnessjoen slide	5	–	2.0	0.7	–	
Grand Banks slide	3	20000	50	16.7–27.7	1000	Fine et al. (2005); Mohrig et al. (1998)
Finneidfjord slide	18	–	1~2	–	1.6	Longva et al. (2003)
Nuuanu slide	0~5	23000	200[a]	50	230	Satake et al. (2002); Moore et al., 1989
El Golfo avalanche	1~10	1500	0~200[a]	–	65	Masson et al. (2006)
Storegga slide	0.05–1.4	95 000	0~430[a]	25–30	810	Haflidason et al. (2004)
Saharan slide	0.05–1.6	48 000	5~40[a]	–	700	Gee et al. (1999)
Canary debris Flow	0.0–1.0	40 000	0~20[a]	50	600	Masson et al. (2006)
Afen slide	0.7–2.5	38	0~8[a]	–	12	Wilson et al., 2004

[a] measured from the mass transport deposits.

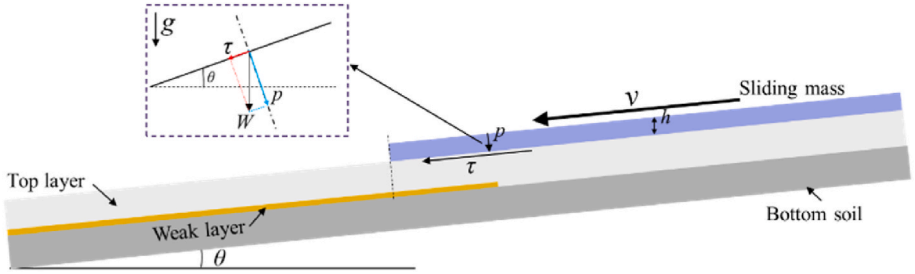

Fig. 2. Sketch showing the studied problem.

$$\tau = \gamma' h \sin\theta \tag{2}$$

Note that the shear resistance (or skin friction) between the seabed and slide mass increases with the travel velocity of the slide mass and reaches the maximum (balancing the shear stress calculated by Eq. (2)) in a quasi-static state. It should be smaller than the undrained shear strength of the sliding mass; otherwise, the shear failure occurs within the sliding mass like a slump. The undrained shear strength of the sliding mass is reported in a range of 0.01 kPa–100 kPa at different flow regimes (Elverhoi et al., 2010; Marr et al., 2002; Whipple, 1997).

3. Numerical modelling

3.1. Finite element model

The numerical models used in the study are shown in Fig. 3. Two models were employed with one for the quasi-static and small-deformation condition (see Fig. 3(a)) and the other for the dynamic and large-deformation condition (see Fig. 3(b)) taking advantages of the Coupled Eulerian-Lagrangian (CEL) method in ABAQUS (Dey and Hawlader, 2015; Wang and Hawlader, 2017). The dynamic model is more realistic considering the dynamics of the sliding mass and the inertia effect of the seafloor sediments. The static model, however, divides the whole dynamic sliding process into different transient

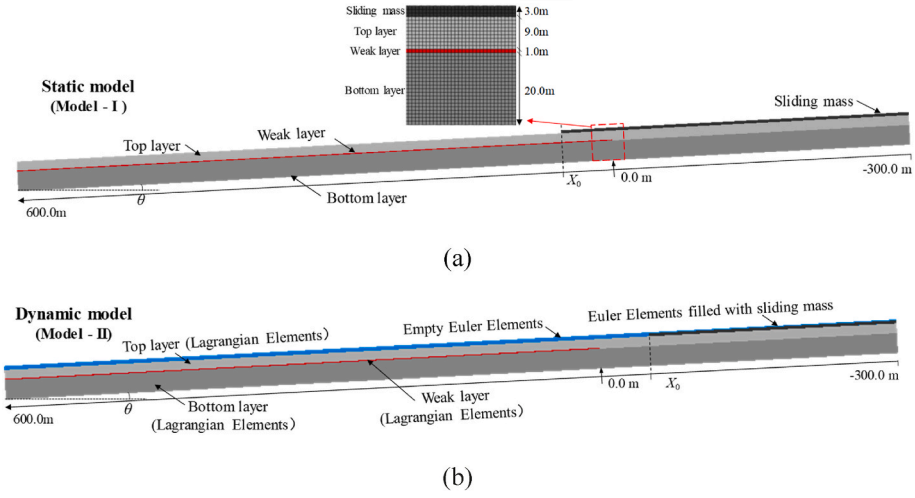

Fig. 3. FE model used in the analysis: (a) static model (Model – I, Lagrangian elements are utilized); (b) dynamic model for the sliding mass propagation (Model – II, the sliding mass filled with Euler elements, while the remaining soils are designated as Lagrangian).

quasi-static stages and the seafloor stability at each transient stage is simulated separately, saving the computational time. Both models comprise a seafloor with a length of 900 m and a thickness of 30 m, inclined at a slope angle of 3° (for the base case) with respect to the horizontal direction. An embedded weak layer of a thickness of 1 m was assumed at a depth of 10 m from the seabed surface. The weak layer is surrounded by stronger materials and truncated at a distance from the left boundary of 300 m. The weak layer was intentionally set to be concentrated in a finite area beyond which the seafloor is sufficiently strong such that the sliding mass may have little impact on the seafloor but with surficial erosions only (Alves, 2015; Alves and Cartwright, 2009; Leshchinsky et al., 2019). While a realistic weak layer may cover a wider area, this setting ensures clear investigations of the initiation of the second failure with or without a weak layer by moving the slide mass from a stronger seafloor segment to a weaker seafloor segment. The origin of the coordinate was put at the end of the weak layer with the downslope direction being positive. The two out-of-plane boundaries were not allowed to move along the out-of-plane direction, simulating the plane strain condition. The bottom boundary was fixed in all directions while the side boundaries were fixed in the slope parallel direction but free to move along the direction perpendicular to the seabed surface.

For the static model (Model-I), 8-noded brick elements of 1 m × 1 m × 1 m were used, and the interface between the seafloor and the sliding mass was considered rough simulating a non-slip boundary condition. The thickness of the sliding mass was set constant as 3.0 m, and the unit weight of soils was various among cases to reflect the effect of different magnitudes of impact from the initial slide.

For a dynamic analysis, the slide mass was released to move along the seafloor surface in a designated velocity with a slip boundary considered. Hereafter, the front of the moving slide mass is denoted as X_0. Different from the static analysis, Eulerian 8-noded brick elements (EC3D8R) were adopted for the slide mass domain in the dynamic analysis, and the inflow Eulerian boundary was used at the right boundary of the slide mass to simulate an infinite slide mass.

3.2. Material parameters

The strain softening behaviour of soils plays a key role in SBP and slab failure in submarine landslides. For the sediments within the top layer and weak layer, a nonlinear post-peak degradation rule was used, given by Einav and Randolph (2005).

$$s_u = \left[\delta_{rem} + (1 - \delta_{rem})e^{-3\delta/\delta_{95}}\right]s_{up} \tag{3}$$

where s_u is the current undrained shear strength; s_{up} is the initial (peak) undrained shear strength with the subscriptions 't' and 'w' denoting the top layer and weak layer, respectively; $\delta_{rem} = 1/S_t = s_{ur}/s_{up}$ (s_{ur} is the residual shear strength) is the inverse of the soil sensitivity; δ is the accumulated plastic shear displacement; and δ_{95} is the value of δ at which the undrained shear strength is reduced by 95%. The value of δ_{95} is in a range of 0.02–1.0 m (Dey et al., 2016a), and was set to 0.2 m for the base case in present study.

The relationship between the plastic shear displacement δ and the plastic shear strain (γ^p) is given by

$$\delta = \gamma^p t \tag{4}$$

where t is the thickness of the shear band. The shear band thickness approximates to the mesh size as only one layer of mesh was set in the weak layer. Therefore, mesh dependency caused by strain softening can be eliminated by fixing the value of $\delta_{95} = \gamma_{95} t$ (0.2 m for the base case here) in spite of the shear band thickness t (Zhang et al., 2015).

No plastic failure was allowed for the sliding mass to maintain its shape. For the seafloor, the initial undrained (peak) shear strength was assumed uniform over the depth and valued at $s_{up,t} = s_{up,w} = 10$ kPa. Therefore, the strength ratio, s_{up}/σ'_{v0}, is 0.14 in the weak layer and averaged at 0.28 in the overlying layer, ensuring the shear band initiation within the weak layer. The Poisson's ratio was set to $\upsilon = 0.495$ to warrantee undrained conditions. The submerged unit weight of seafloor sediments was fixed to $\gamma' = 7.84$ kN/m^3; while different values were considered for the sliding mass to achieve different magnitudes of impact force. In the dynamic analysis, the viscous damping is incorporated using the Rayleigh method. The mass damping was nil and the stiffness damping with $\beta = 0.000375$ was used, which is in accordance with Wang et al. (2019). Main soil parameters used in the numerical modelling are listed in Table 2.

3.3. Model verification

To verify the numerical model, the problem described above was modified by removing the sliding mass and introducing a pre-softened zone at the middle of the weak layer to trigger failure, whereby the critical length of the pre-softened zone for catastrophic failure is given by (Zhang et al., 2015)

$$l_{cr} = \sqrt{1 - r(1 - \ln r)}\ \frac{2l_u}{r} \tag{5}$$

where l_{cr} is the critical length of the pre-softened zone, r is the shear stress ratio, and l_u is the characteristic length given by (Puzrin et al., 2004; Zhang and Wang, 2015)

$$l_u = \sqrt{\frac{2E_{ps}\delta_{95}h_w}{3(s_{up} - s_{ur})}} \tag{6}$$

where $E_{ps} = E/(1\text{-}\upsilon^2)$ is the plane strain modulus, h_w the depth of the weak layer, and υ the Poisson's ratio. The shear stress ratio is calculated by

$$r = \frac{\tau_g - s_{ur}}{s_{up} - s_{ur}} \tag{7}$$

where $\tau_g = \gamma' h_w \sin\theta$ ($h_w = 9.5$ m is the sum of the thicknesses of the top layer – 9 m, and half of the weak layer – 0.5 m) is the averaged gravitational shear stress within the weak layer.

The formation of the pre-softened zone might be due to external factors such as existence of an artesian aquifer (Zhang et al. 2020), which may finally lead to SBP in the weak layer and global failure in the overlying layer upon critical length given by equation (5). With parameters listed in Table 2, the values of r and l_u are 0.238 m and 25.08 m, respectively, and the critical pre-softened zone length is hence l_{cr} = 136.7 m based on Eq. (5).

Table 2
The basic soil parameters used in the analysis.

Parameters	Downslope seafloor			Sliding mass
	Top layer	Weak layer	Bottom layer	
Peak undrained shear strength s_{up}: kPa	10	10	–	–
Thickness, m	9	1	25	3
Young's modulus, E: kPa	3000	3000	3000 + 300z[a]	750
Poisson's ratio, υ	0.495	0.495	0.495	0.495
Submerged unit weight, γ': kN/m3	7.84	7.84	7.84	2.4–13.7
Strain softening parameters (S_t and δ_{95})	–	($S_t = 5.0$, $\delta_{95} = 0.2$ m)	–	–
Rayleigh damping parameter (–dynamic analysis), β	0.000375	0.000375	–	–

Note.
[a] means the value of E increases with the depth z.

As shown in Fig. 4(a)–a numerical slope with the slope angle of 3° and length of 500.0 m was used. The pre-softened zone was gradually increased until obvious SBP and hence catastrophic failure were observed in the numerical modelling. In the pre-softened zone, the soils were assumed at the residual state.

As shown in Fig. 4(b), when the length of the pre-softened zone, L_0, is 135 m, the slope remains stable even for a large analysis time of $t = 100$ s. However, as the length of the fully softened zone increases to 136 m, the shear band propagates along the weak layer both upslope and downslope, and a global slab failure with failure propagation to seafloor surface occurs at the final state as shown in Fig. 4(c). The good agreement between the numerical and analytical results in terms of the critical pre-softened zone length indicates that the used numerical model can simulate the submarine landslide initiation with SBP.

4. Numerical results and discussions

4.1. Seafloor failure mechanisms under impact of initial slide

Subsequent failures might follow the initial slide with retrogression upslope or ploughing downslope (Zhang and Wang, 2019). A particular downslope seafloor failure, with new SBP along an underlying weak layer under the impact of the sliding mass, is presented here. As a first step, the sliding mass impacting the intact seafloor is simplified as a total impact load ignoring any inertia effect (see the static model in Fig. 3(a)), which corresponds to the stages when the sliding mass moves in a steady velocity or re-stabilizes at the final phase of the slide. A few factors, such as the sliding mass weight and position, the seafloor inclination, and the soil parameters of seafloor sediments, may affect the subsequent failure initiation and mechanism. A parametric study was conducted to explore the controlling parameters as shown in Table 3.

For the case study, the thickness of the sliding mass (h) was set to 3 m which results in the total impact load (unit-area load) of $W = \gamma' h = 24.5$ kPa. As the sliding mass moves from $X_0 = -50.0$ m to 10m, the plastic strain in the weak layer is limited although gradually developed, and the seafloor remains stable, as shown in Fig. 5.

When the sliding mass front arrives at $X_0 = 50.0$ m, however, the shear band propagates catastrophically in the weak layer with the length

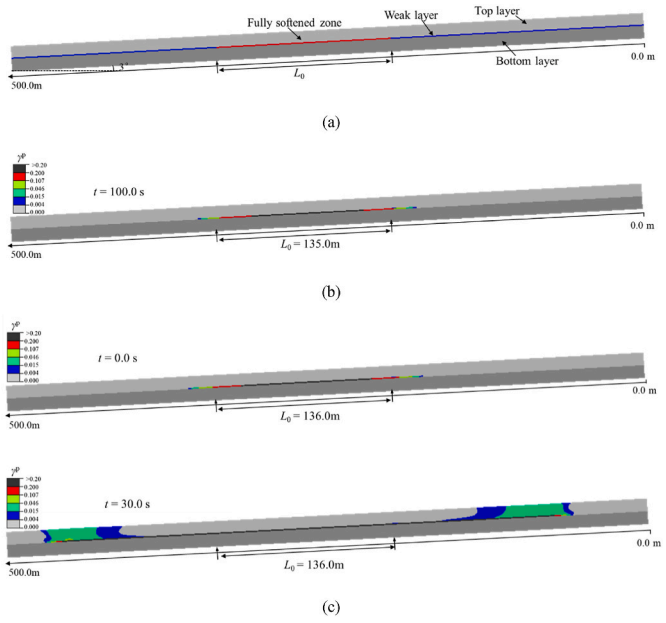

Fig. 4. The verification of the numerical model with respect to the SBP in an infinite slope (Zhang et al. 2020): (a) the initial numerical model (by using Lagrangian elements); (b) the SBP with the pre-softened zone length $L_0 = 135.0$ m (c) the SBP with $L_0 = 136.0$ m at different times.

Table 3
Valus used for the parametric study in the analysis.

Model type	Downslope seafloor				Sliding mass	
	Slope angle, θ (°)	$s_{up,w}/s_{up,t}$	S_t	δ_{95} (m)	Load boundary, X_0, (m)	Velocity, v (m/s)
Static	3	1	5	0.2	−50, −40, −30, −20, −10, 0, 10, 20, 30, 40, 50, 150	0
	3	0.5, 0.6, 0.7, 0.8, 0.9, 1.0	5	0.2	50	0
	3	1.0	3, 5, 8, 10, 20	0.2	50	0
	3	1.0	5	0.02, 0.2, 0.4, 0.8, 2.0	50	0
	2, 3, 5, 7	1	5	0.2	−50 - changeable	0
Dynamic	3	0.5, 0.6, 0.7, 0.8, 0.9, 1.0	5	0.2	−50 - changeable	0.5, 5

increasing to about 100 m within 20 s, followed by slab failure in the top layer of the seafloor as shown in Fig. 6. The slab failure with SBP is extended both downslope and upslope with the failure length exceeding 300 m at $t = 29$ s. By this time, large deformation has been accumulated in the top layer, which is deemed resulting in a larger landslide. Thus, the sliding mass of $W = 24.5$ kPa is sufficient to trigger a significant downslope seafloor failure with the presence of a weak layer as depicted.

To further investigate the failure mechanism for the case with the sliding mass front at $X_0 = 50$ m, Fig. 7(a) shows the evolution of the shear stress in the weak layer, while Fig. 7(b) presents the evolution for the degree of softening which is calculated as $(s_{up,w}\text{-}s_u)/(s_{up,w}\text{-}s_{ur,w})$. At the initial state, the gravity shear stress (τ_g) is constant over the weak layer and less than the peak shear strength. Hence, there is no strain softening observed at the beginning. With the sliding mass moving downward, the shear stress in the weak layer is gradually increased. The peak shear stress is mobilized at $X_0 = 50$ m, even with a reduced transient impact of $0.73W$. With the increase of the transient load (by increasing the submerged density of the sliding mass) to the target W, the plastic displacement is gradually accumulated in the weak layer with a concentration at $X_0 = 50$ m, where the shear strength and hence the shear stress begin to reduce from the peak strength ($s_{up,w}$) towards the residual strength ($s_{ur,w}$). Thereafter, the shear band propagates progressively along the weak layer. Once the sliding mass has fully landed on the seafloor with the total impact load of W, the SBP becomes catastrophic and the global slope failure is formed.

A different seafloor failure mechanism might be apparent when the sliding mass unit weight increases to $W = 41.2$ kPa as shown in Fig. 6(b). With a thicker sliding mass, the global seafloor failure might occur even without the presence of the weak layer, and the failure is localized at the front of the sliding mass with a wedge shape. This failure mechanism is analogy to the embankment failure in a uniform clay ground as discussed in many previous studies (e.g., Andresen and Jostad, 2007; Dey and Hawlader, 2016b; Wang and Hawlader, 2017), which is referred to as the erosion failure mechanism in the remaining of the paper.

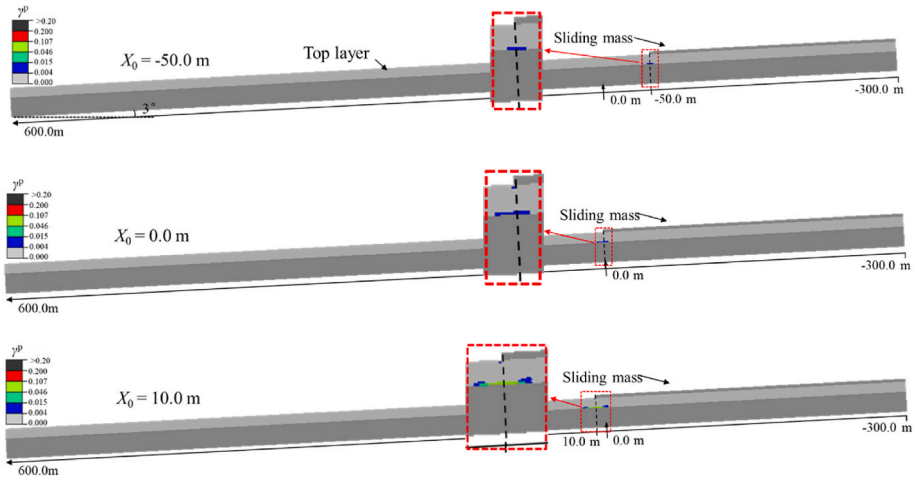

Fig. 5. SBP for the sliding mass front at different positions of the seafloor (total impact load from the sliding mass, W = 24.5 kPa).

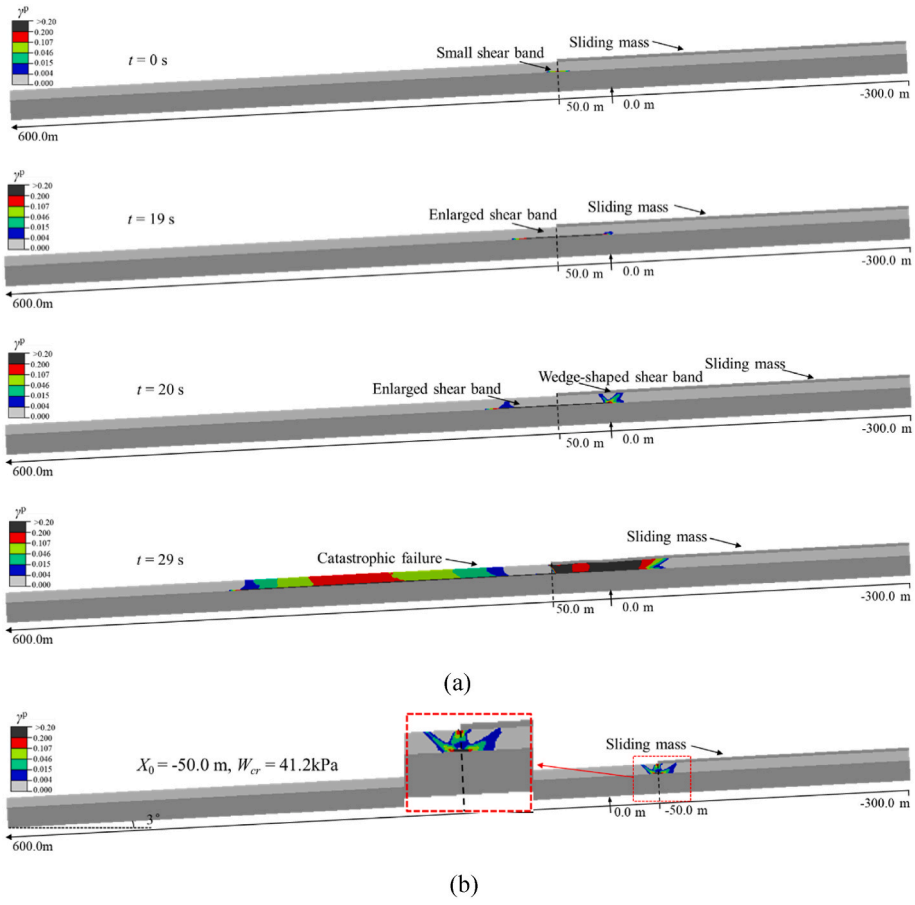

Fig. 6. Different failure mechanisms for cases of S_t = 5.0 and δ_{95} = 0.2 m at the critical load condition: (a) SBP along the weak layer with the sliding mass front X_0 = 50.0 m (W_{cr} = 24.5 kPa); (b) erosion failure mechanism with the sliding mass front X_0 = −50.0 m (W_{cr} = 41.2 kPa).

4.2. Critical impact load from the sliding mass

According to the above analysis, the failure mechanism of the downslope seafloor impacted by the initial slide might be different with different magnitudes of the impact load from the sliding mass. For a thicker (or heavier) sliding mass, seafloor failure is in a similar way to the embankment failure regardless the presence of a weak layer. For a thinner (lighter) sliding mass, however, seafloor failure is accompanied by progressive SBP in the underlying weak layer. It is therefore important to understand the critical impact load for each of the failure mechanism. The critical impact load was determined here by gradually increasing the unit weight of the sliding mass until the global seafloor failure was triggered. This was fulfilled by adjusting the density of the sliding mass but fixing the thickness (h = 3.0 m).

The critical impact loads against different positions of the sliding mass front are presented in Fig. 8. For the erosion failure mechanism without the presence of the weak layer, the critical impact load from the sliding mass (or the critical weight per length, W_{cr}) needs to be as high as

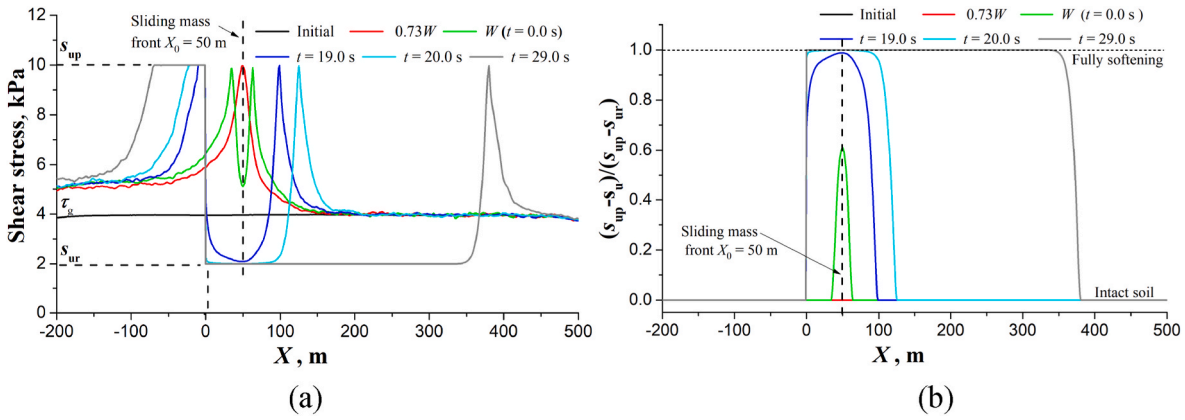

Fig. 7. Evolutions of (a) the shear stress distribution; and (b) the degree of softening (with the value zero and unity mean the no softening and full softening, respectively) during SBP for a typical static case with the sliding mass front $X_0 = 50$ m.

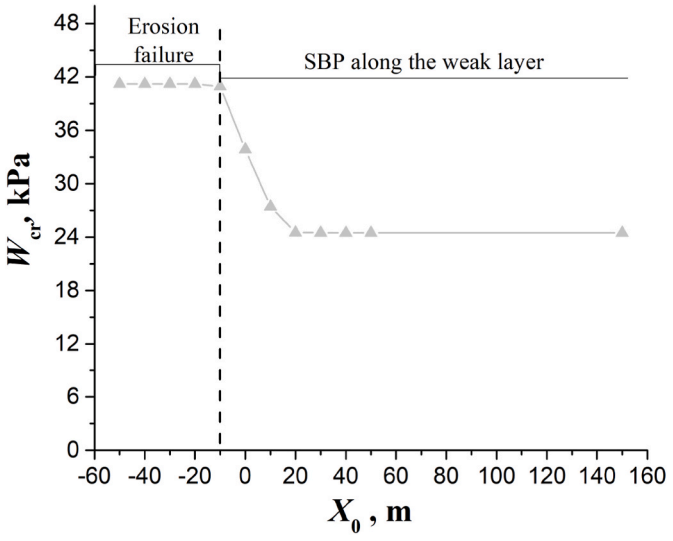

Fig. 8. The critical loads (W_{cr}) at different positions of the sliding mass front (X_0).

41.2 kPa. For the failure with SBP when the sliding mass is above the seafloor with the weak layer, the critical weight (W_{cr}) reduces to 24.5 kPa. For the cases with X_0 various from −10 m to 20 m, the critical impact load gradually decreases from 41.2 kPa to 24.5 kPa, as the failure mechanism transits from the surficial erosion to the SBP dominant. The minimum critical impact load, corresponding to the failure mechanism with SBP, is hereafter referred to as the critical impact load unless otherwise specified.

4.3. Controlling factors for seafloor failure impacted by initial slide

In this section, the factors controlling the seafloor failure and the critical impact load are discussed. The failure with SBP is inherently related to the strain softening parameters (i.e., the soil sensitivity S_t and the residual plastic shear displacement δ_{95} according to Eq. (3)). In addition, the failure is influenced by the driving force, as opposed to the resistance in the weak layer (acting as the basal shear surface), governed by the overlying layer soils and the sliding mass. As an additional driving force, the impact load from the sliding mass is normalized as the transient shear stress ratio on the weak layer, given by

$$r_w = \frac{W \sin\theta}{s_{up,w} - s_{ur,w}} \tag{8}$$

4.4. Strain softening parameters

The effects of the strain softening parameters, i.e., the soil sensitivity and residual plastic shear displacement, are first studied. The marine soil sensitivity usually ranges between 3 and 6 (Randolph and Gourvenec, 2011) and is reported to be less than 20.0 (Y. Ren et al., 2019). Fig. 9(a) shows the critical impact loads and the critical apparent shear stress ratios at different values of soil sensitivity from 3 to 20. Note that, in all cases, other parameters are the same with the base case. With the soil sensitivity falling in the normal range (i.e. 3 - 6), the critical impact load required for secondary failure decreases with the increase of the soil sensitivity. When S_t is greater than 6, however, the critical impact load and the transient shear stress ratio are little affected.

The residual plastic shear displacement, δ_{95}, is a parameter related to the soil brittleness and in a range of 0.02–1.0 m for Canadian quick clays (Quinn et al., 2011). As shown in Fig. 9(b), the critical impact load and the transient shear stress ratio increase with the increase of δ_{95} implying that more brittle marine sediments are more prone to collapse.

4.5. Weak layer strength

As observed above, the presence of the weak layer has a significant effect on the seafloor instability under the impact of the initial slide. The seafloor stability therefore depends on how 'weak' the basal shear surface is compared to the adjacent layers. A parametric study was conducted with respect to the ratio of strengths between the weak layer and overlying (top) layer, i.e. $s_{up,w}/s_{up,\ t}$. With the ratio increasing from 0.5 to 1, the critical impact load, W_{cr}, is significantly increased from around 5.4 kPa–24.5 kPa as shown in Fig. 9(c). Correspondingly, the critical transient shear stress ratio increases from 0.07 to 0.16.

4.6. Seafloor inclination

Weak layers are usually observed or assumed parallel to the seafloor surface due to the geological sedimentation history. The seafloor inclination, which affects the gravity shear stress in the weak layer, hence influences the seafloor stability. A parametric study was conducted with the seafloor inclination ranging from 2° to 7°. The critical impact loads and transient shear stress ratios at different seafloor inclinations are presented in Fig. 9(d). As observed in the figure, the seafloor inclination has significant effects on the critical impact load and transient shear stress ratio. The value of W_{cr} decreases from 33.4 kPa to 3.0 kPa as the inclination increases from 2° to 7°. The value of r_w slightly increases as the inclination increasing from 2° to 3°, but decreases from 0.16 to 0.05 with the inclination further increasing from 3° to 7°.

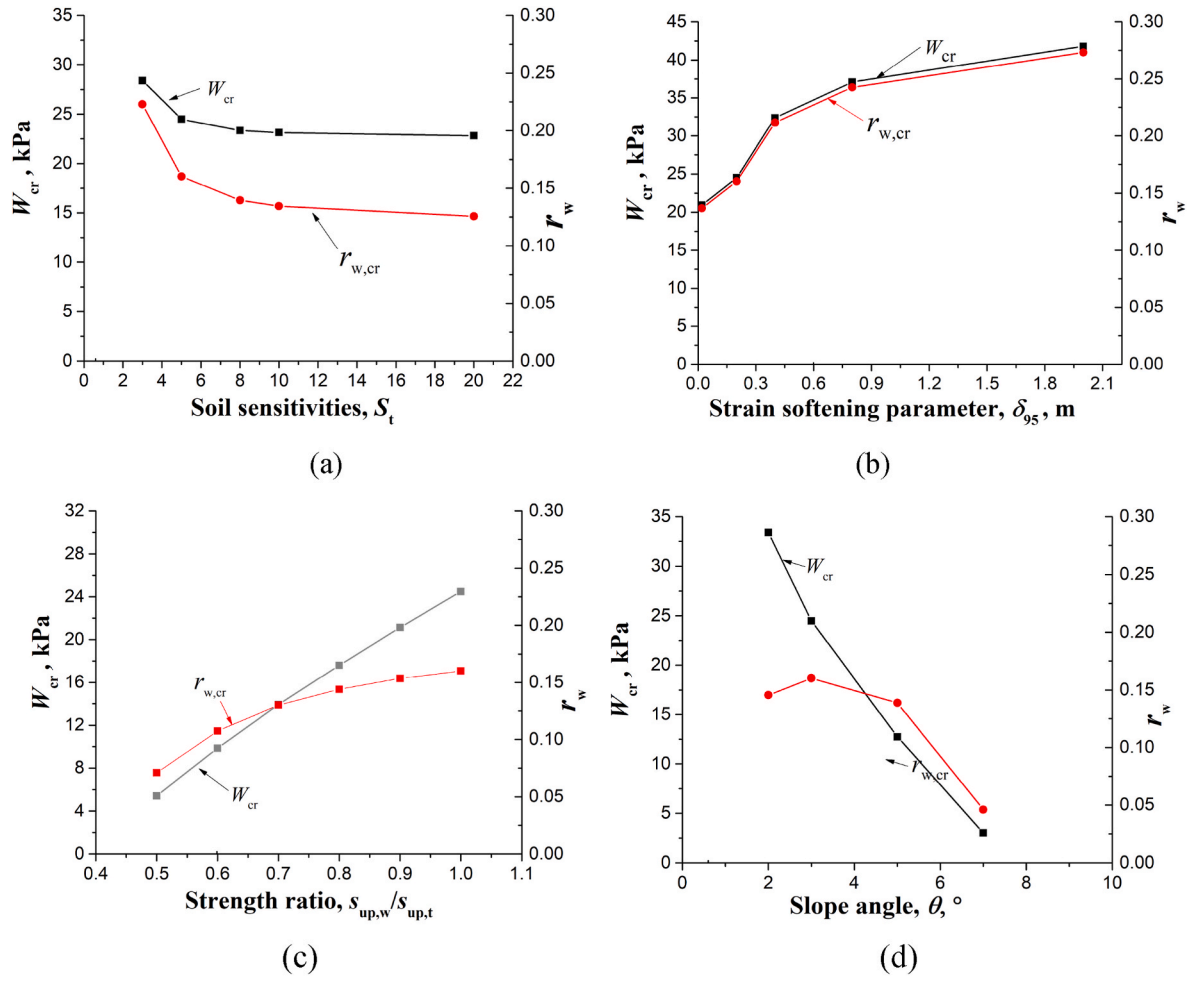

Fig. 9. Parametric studies of controlling factors for downslope seafloor failure by the initial slide: (a) S_t ($\delta_{95} = 0.2$ m); (b) δ_{95}, m ($S_t = 5.0$); (c) strength ratio ($s_{up,w}/s_{up,t}$) ($S_t = 5.0$, $\delta_{95} = 0.2$ m); (d) slope angle (θ, °) ($s_{up,w}/s_{up,t} = 1.0$, $S_t = 5.0$, $\delta_{95} = 0.2$ m).

4.7. Seabed skin friction

In the above sections, a non-slip interaction between the sliding mass and the seafloor surface was assumed. The shear resistance increases with the travel velocity and reaches the maximum equalling the shear stress (calculated by Eq. (2)) from the slide mass in the quasi-static state where the travel velocity is the constant. Such that, the values of the overburden pressure and shear resistance are coupled by $\tau = p\tan\theta$. However, the skin friction might be less than the value calculated by Eq. (2), due to either the existence of a slip interface or lower shear strength than the gravity shear stress in the sliding mass. With the latter, the shear failure occurs inside the sliding mass with a boundary shear layer of certain thickness.

To analyse the respective effects of the two stress components on the seafloor stability, a simplified static model was used in this section where the two stress components (p and τ) were decoupled as shown in Fig. 10(a). To verify this decoupled model, in the first analysis, the values of p and τ were calculated based on equations (1) and (2), respectively. Fig. 10(b) shows the distributions of shear stress on the weak layer by different loading scenarios, which implies that: a) the increase of shear stress at the sliding mass front is mainly caused by the overburden pressure p; b) the component τ dominantly affects the weak layer shear stress behind the sliding mass front, and c) the shear stress distribution in the decoupled model with separate contributions from p and τ is identical to the rigorous static model with a non-slip interface.

To study the contribution of τ, two situations, i.e., non-slip and slip boundary conditions, were considered in this section. The shear resistance or skin friction was set to zero for the slip boundary condition. Fig. 10(c) presents the critical impact loads against different values of $s_{up,w}/s_{up,t}$ for these two limits. The critical impact load increases with the value of $s_{up,w}/s_{up,t}$ in spite of the interface boundary condition, and the interface boundary condition has a limited effect on the critical impact load. The value of W_{cr} with the slip interface is up to 19.7% larger than that with the non-slip interface.

4.8. Criterion for downslope seafloor instability by sliding mass

According to the above parametric studies, the value of $s_{up,w}/s_{up,t}$ have a significant effect on W_{cr}; while the soil sensitivity (S_t) has little effect on the results. This indicates, to assess the seafloor instability by the initial slide, accurate measurement of strength profiles is of importance. Based on the collective numerical data shown in Fig. 11, an empirical relationship between the critical transient shear stress ratio ($r_{w,cr}$, representing the additional driving force from the sliding mass) and the shear stress ratio (r, representing the initial driving force from the seafloor gravity) in the weak layer can be expressed by

$$r_{w,cr} = \frac{W_{cr}\sin\theta}{s_{up,w} - s_{ur,w}} = 0.2 - 0.17r\left(R^2 = 0.79\right) \tag{9}$$

From Eq. (9), the higher the shear stress ratio (r, for pessimistic seafloors) is, the lower the critical transient shear stress ratio is required for triggering seafloor instability. One of the advantages of the proposed empirical equations lies in their easy application in practical seabed instability analysis. Subsequent failure within the downslope weak layer

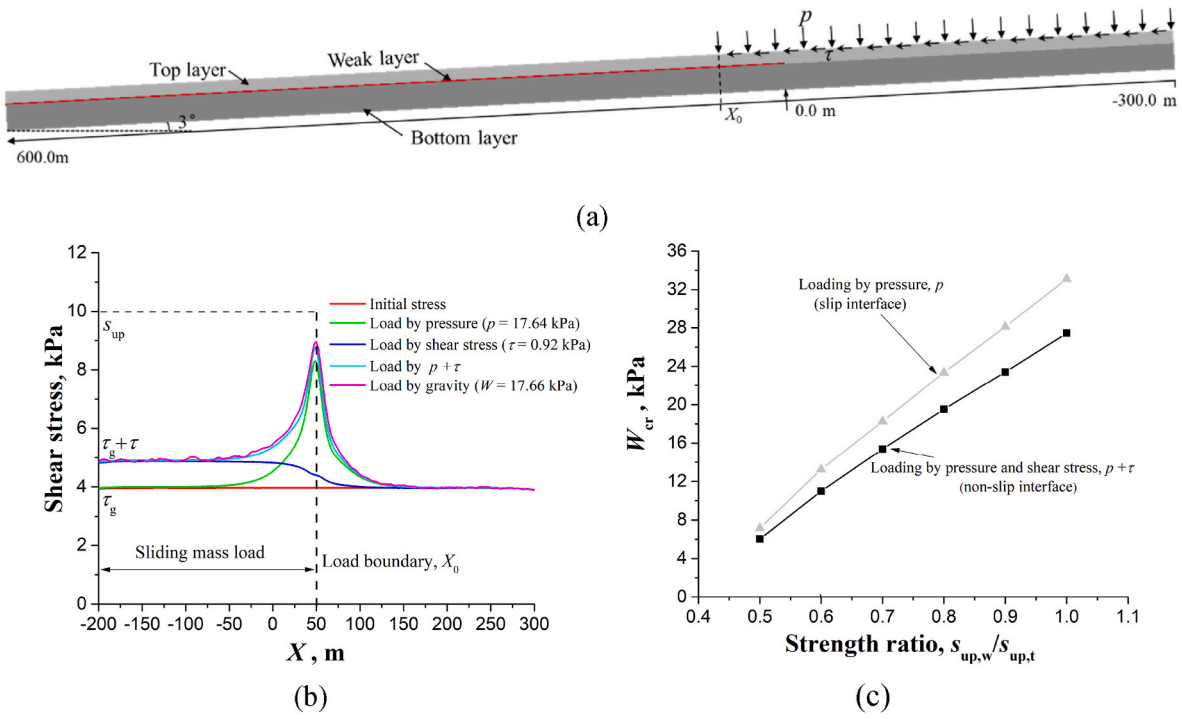

Fig. 10. The effect of the seafloor surface – sliding mass friction on downslope seafloor failure by the initial slide: (a) the simplified model; (b) the shear stress distributions in the weak layer with W = 17.66 kPa; and (c) critical loads (W_{cr}) for both no-slip and slip interfaces against different strength ratios.

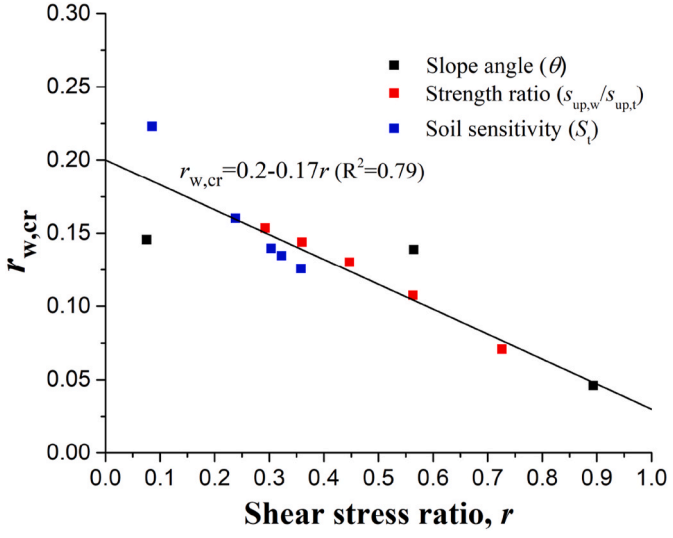

Fig. 11. Critical values of the normalized impact load ($r_{w,cr}$) from the sliding mass against shear stress ratios in the weak layer of the seafloor.

is expected to occur if the driving force parameter r_w exceeds the critical resistance parameter $r_{w,cr}$. The values of r_w and $r_{w,cr}$ can be computed based on the geometry and soil properties of the first slide and the downslope weak layer, respectively, as shown in Fig. 12.

4.9. Dynamic effects

In the above ideal static analysis, the total impact load of the sliding mass was applied on the seafloor, whereby the failure is initiated at the current front of the sliding mass. The footprints (accumulated plastic strains) of the travelling slide mass are ignored. Meanwhile, the static model does not take any inertia effect into account. In this section, the seafloor stability with SBP under the impact of the initial slide is further discussed with respect to the dynamic effects of the moving sliding mass, employing the CEL approach as shown in Fig. 3(b).

In the first case, the sliding mass is virtually put at the seafloor with the front at X_0 = 50 m, which is the same with the base static case. The critical impact load is W_{cr} = 23.85 kPa which is only 2.6% smaller than the static case, verifying the CEL model. Then, in the following cases, the sliding mass front is initially set at X_0 = −50 m and the sliding mass is forced to move along the seabed surface with a constant velocity.

With a velocity of v = 0.5 m/s, the critical impact load with the dynamic effects is W_{cr} = 20.7 kPa, which is considerably (around 13%) lower than the static case. Fig. 13(a) and (b) present the evolutions of the

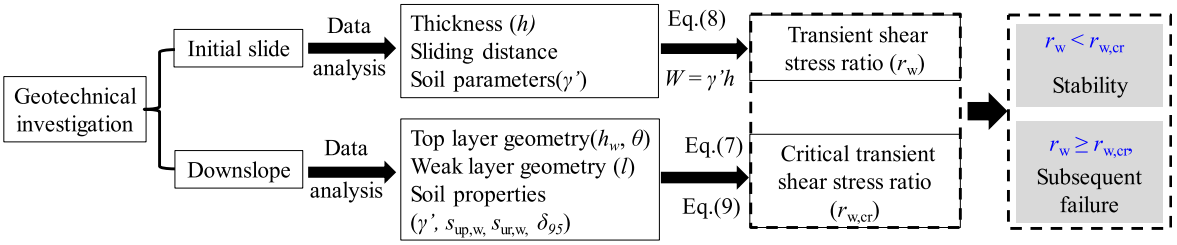

Fig. 12. Procedure to estimate if the subsequent downslope failure can be triggered in practical slope stability assessments.

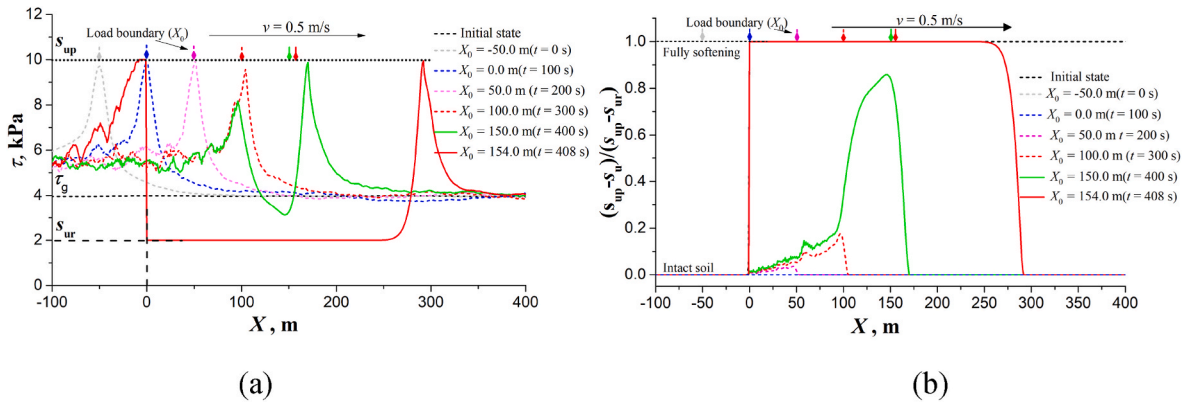

Fig. 13. Evolutions of (a) the shear stress distribution and (b) the degree of softening (with the value zero and unity mean no softening and full softening, respectively) during shear band propagation in the weak layer for the dynamic case of $v = 0.5$ m/s and $W_{cr} = 20.7$ kPa.

shear stress distribution and the degree of softening, respectively, during the movement of the sliding mass. The accumulation of the plastic strain along the weak layer at different stages is indicated in Fig. 14.

When the sliding mass travels along the stronger seafloor segment (i.e. $X_0 < 0$), the seafloor remains intact although the transient shear stress at the sliding mass front approaches the peak value. Once the sliding mass moves into the weak layer region, the transient impact load (concentrated at the sliding mass front) results in plastic failure and strength reduction within the weak layer. When the sliding mass front reaches $X_0 = 50$ m, a considerable amount of plastic strain has been accumulated behind the sliding mass with the current shear strength less than the peak behind the sliding mass front. This certainly makes the seafloor more prone to collapse compared to the static model where the seafloor sediments remain intact before applying the sliding mass impact load.

With the sliding mass moving forward, the plastic strains are continuingly accumulated, and the strain softening becomes significant in the weak layer. A fully softened zone forms with the shear strength

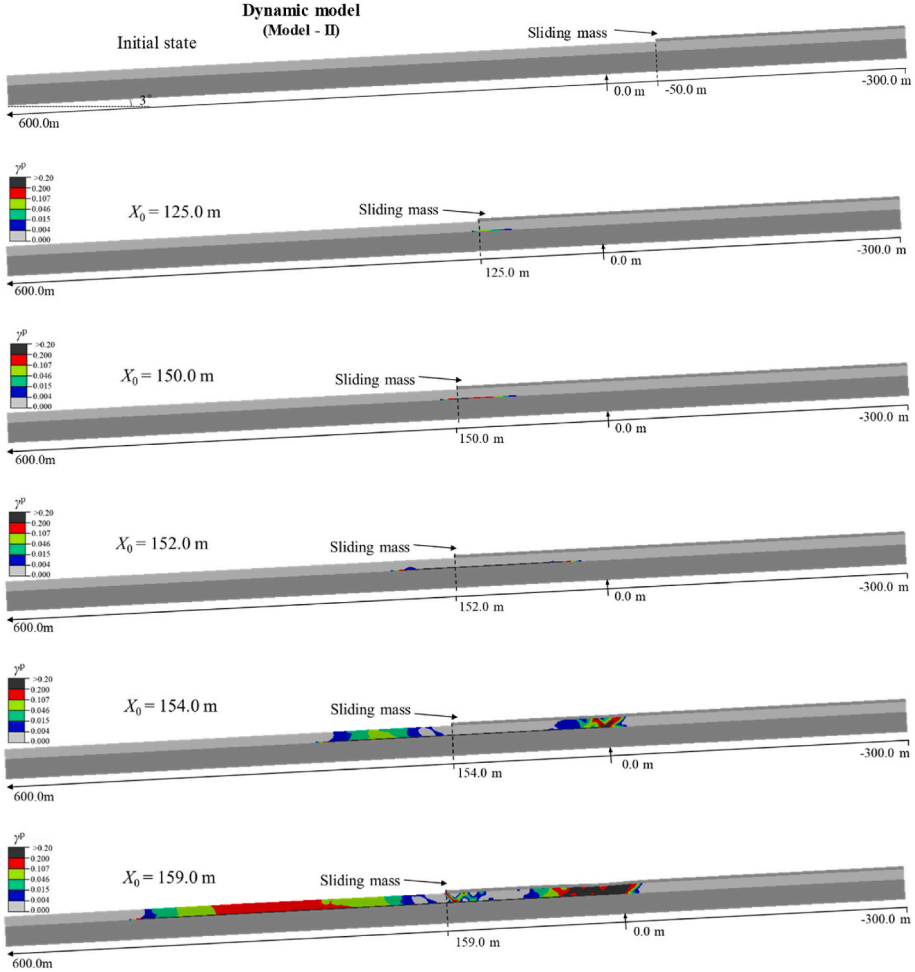

Fig. 14. Shear band propagation along the weak layer at different times (and hence different positions of the sliding mass front) based on the dynamic model (Model II), the case with $v = 0.5$ m/s and $W_{cr} = 20.7$ kPa.

reduced to the residual when the sliding mass front arrives at $X_0 = 152$ m. Thereafter, catastrophic SBP dominates the slab failure when the sliding mass front is at $X_0 = 154$ m. As shown in the bottom sub-plot of Fig. 14, the downslope failure extent because of SBP is far ahead of the sliding mass front forming a much larger scale of failure.

To analyse the effect of the speed of the sliding mass on the seafloor stability, two series of numerical cases were conducted with the sliding mass velocity being $v = 0.5$ m/s and 5.0 m/s, respectively. The critical impact loads against different values of gravity shear stress ratio, r, are presented in Fig. 15 for both series. The critical loads with $v = 0.5$ m/s are only up to 2.4% smaller than those with $v = 5.0$ m/s, which shows that the velocity of the sliding mass has little effect on the result. However, compared to the data from the static model, the critical impact loads with the dynamic model are around 15% lower, which means the footprint of the slide mass has a significant influence on the seafloor stability.

5. Conclusions

The huge volumes of many submarine landslides have suggested subsequent failure of upslope and downslope seafloor caused by an initial smaller slide. The study has focused on the second failure and post-failure behaviours of the downslope seafloor with the presence of a weak layer impacted by the initial slide. The sliding mass from the first failure may act as an impact load on the seafloor that it comes across which may potentially leads to collapse of the seafloor, especially when a weak layer is embedded. This second and/or the subsequent failure may hence escalate the scale of a submarine landslide. A large deformation finite element (LDFE) modelling has been carried out to observe the progressive seafloor failure by the impact of the slide mass. The strain softening phenomenon has been considered for the marine sediments in the weak layer. The failure mechanisms and controlling factors of downslope seafloor impacted by the first failure have been revealed, and an original criterion has been proposed for assessing the secondary failure of downslope seafloor. Main conclusions are drawn below.

Two failure mechanisms of downslope seafloors impacted by the slide mass of the first failure have been proposed. The seafloor remains stable if it is impacted by a light initial slide mass (a low-density turbidity or slender debris flow) potentially resulting in surficial erosion. Impacted by a heavy slide mass (a thick slide or debris flow), however, the concentrated shear stress at the slide mass front may exceed the peak shear strength in the weak layer, leading to strength reduction during further shearing. Subject to sufficient accumulation of plastic strains or a very heavy slide mass, the soils in the weak layer might be fully softened with catastrophic shear band propagation (SBP). Seafloor collapses with extensive compression and thrust, forming failed blocks. This failure mechanism may help explain some large-scale submarine landslides with multistage failure.

The impact load from the initial slide can be divided into two components: the pressure normal to the seafloor and the shear stress parallel to the seafloor. It is found in the study that the potential seafloor instability is mainly caused by the normal pressure which causes a stress concentration at the slide mass front. The critical condition for the SBP caused seafloor instability is governed by both the impact load from the initial slide and the gravity load relative to the shear strength in the weak layer. An empirical equation (see Equation (9)) for assessing the SBP caused seafloor instability subjected to the initial slide, with respect to these two factors, has been proposed based on the numerical data.

A parametric study has been conducted to study the controlling factors for the seafloor instability under the impact of the initial slide. The numerical modelling shows the strain softening parameters and the shear strength in the weak layer relative to that in the overlying seafloor have far-reaching effects on the seafloor instability. The weaker and more brittle the materials in the weak layer are, more prone to failure the seafloor is. Meanwhile, the critical impact load of the slide mass for triggering the seafloor instability decreases with the increase of the soil sensitivity. However, the dynamic inertia has little effect on the critical impact load.

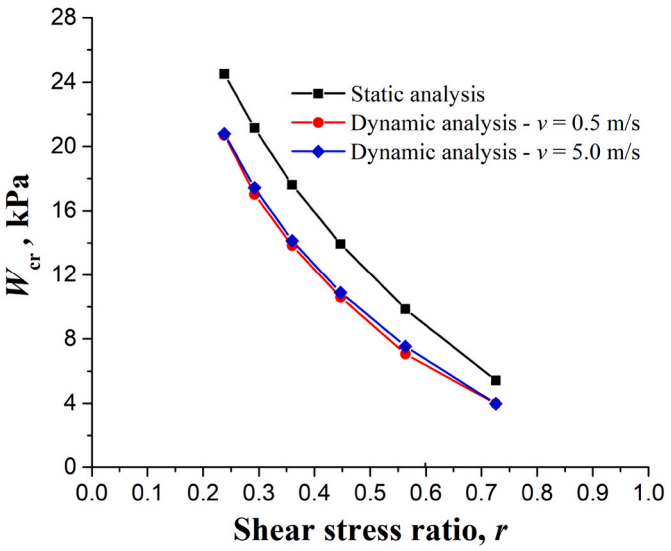

Fig. 15. A comparison of the critical loads of the sliding mass between the static and dynamic analyses (with the slope angle $\theta = 3°$).

CRediT authorship contribution statement

Yunrui Han: Writing – review & editing, Writing – original draft, Validation, Software, Methodology, Investigation, Formal analysis. **Wangcheng Zhang:** Writing – review & editing, Supervision, Methodology, Investigation, Conceptualization. **Long Yu:** Writing – review & editing, Supervision, Project administration, Funding acquisition. **Zhongtao Wang:** Writing – review & editing. **Qing Yang:** Writing – review & editing, Supervision, Funding acquisition.

Declaration of competing interest

The authors declare that they have no known competing financial interests or personal relationships that could have appeared to influence the work reported in this paper.

Data availability

Data will be made available on request.

Acknowledgements

The study is financial supported by the National Natural Science Foundation of China (Grant nos. 52109115, 52171252 and 52331010), Liaoning Province Doctoral Research Startup Fund Program (2022BS082) and the Fundamental Research Funds for the Central Universities (DUT23RC(3)018). The first author acknowledges the support from the China Scholarship Council for a 12-month secondment at the University of Western Australia. The authors would thank Prof. Mark Randolph of the University of Western Australia for valuable discussions on the topic.

Appendix A. Supplementary data

Supplementary data to this article can be found online at https://doi.org/10.1016/j.oceaneng.2024.117469.

References

Acosta, E.A., Tibana, S., de Almeida, M.d.S.S., Saboya Jr., F., 2017. Centrifuge modeling of hydroplaning in submarine slopes. Ocean Eng. 129, 451–458.

Alves, T.M., 2015. Submarine slide blocks and associated soft-sediment deformation in deep-water basins: a review. Mar. Petrol. Geol. 67, 262–285.

Alves, T.M., Cartwright, J.A., 2009. Volume balance of a submarine landslide in the Espírito Santo Basin, offshore Brazil: quantifying seafloor erosion, sediment accumulation and depletion. Earth Planet Sci. Lett. 288 (3–4), 572–580.

Andresen, L., Jostad, H.P., 2007. Numerical modeling of failure mechanisms in sensitive soft clay-Application to offshore geohazards. In: Offshore Technology Conference. Houston, Texas, U.S.A.

Bernander, S., 1978. Brittle Failures in Normally Consilidated Soils. Väg-och Vattenbyggaren.

Bernander, S., Kullingsjö, A., Gylland, A.S., Bengtsson, P.-E., Knutsson, S., Pusch, R., et al., 2016. Downhill progressive landslides in long natural slopes: triggering agents and landslide phases modeled with a finite difference method. Can. Geotech. J. 53 (10), 1565–1582.

Boukpeti, N., White, D., Randolph, M., Low, H., 2012. Strength of fine-grained soils at the solid–fluid transition. Geotechnique 62 (3), 213–226.

Bryn, P., Berg, K., Forsberg, C.F., Solheim, A., Kvalstad, T.J., 2005. Explaining the storegga slide. Mar. Petrol. Geol. 22 (1–2), 0-19.

Bugge, T., Belderson, R., Kenyon, N., 1988. The storegga slide. Phil. Trans. Roy. Soc. Lond. Math. Phys. Sci. 325 (1586), 357–388.

Casalbore, D., Bosman, A., Chiocci, F.L., 2012. Study of recent small-scale landslides in geologically active marine areas through repeated multibeam surveys: examples from the southern Italy. In: Submarine Mass Movements and Their Consequences: Advances in Natural and Technological Hazards Research. Springer Netherlands, Kiel, Germany, pp. 573–582.

Casalbore, D., Passeri, F., Tommasi, P., Verrucci, L., Bosman, A., Romagnoli, C., Chiocci, F.L., 2020. Small-scale slope instability on the submarine flanks of insular volcanoes: the case-study of the Sciara del Fuoco slope (Stromboli). Int. J. Earth Sci. 109, 2643–2658.

Dan, G., Sultan, N., Savoye, B., 2007. The 1979 Nice harbour catastrophe revisited: trigger mechanism inferred from geotechnical measurements and numerical modelling. Mar. Geol. 245 (1–4), 40–64.

De Blasio, F.V., Engvik, L., Harbitz, C.B., Elverhøi, A., 2004. Hydroplaning and submarine debris flows. J. Geophys. Res. 109, C01002.

Dey, R., Hawlader, B., Phillips, R., Soga, K., 2015. Large deformation finite-element modeling of progressive failure leading to spread in sensitive clay slopes. Geotechnique 65 (8), 657–668.

Dey, R., Hawlader, B., Phillips, R., Soga, K., 2016a. Modeling of large-deformation behaviour of marine sensitive clays and its application to submarine slope stability analysis. Can. Geotech. J. 53 (7), 1138–1155.

Dey, R., Hawlader, B., Phillips, R., Soga, K., 2016b. Numerical modeling of combined effects of upward and downward propagation of shear bands on stability of slopes with sensitive clay. Int. J. Numer. Anal. Methods GeoMech. 40 (15), 2076–2099.

Dey, R., Hawlader, B., Phillips, R., Soga, K., 2016c. Numerical modelling of submarine landslides with sensitive clay layers. Geotechnique 66 (6), 454–468.

Early, K.R., Skempton, A.W., 1972. Investigations of the landslide at Walton's Wood, staffordshire. Q. J. Eng. Geol. Hydrogeol. 5 (1–2), 19–41.

Einav, I., Randolph, M.F., 2005. Combining upper bound and strain path methods for evaluating penetration resistance. Int. J. Numer. Methods Eng. 63 (No. 14), 1991–2016.

Elverhoi, A., Breien, H., De Blasio, F.V., Harbitz, C.B., Pagliardi, M., 2010. Submarine landslides and the importance of the initial sediment composition for run-out length and final deposit. Ocean Dynam. 60 (4), 1027–1046.

Elverhøi, A., Norem, H., Andersen, E., Dowdeswell, J., Fossen, I., Haflidason, H., et al., 1997. On the origin and flow behavior of submarine slides on deep-sea fans along the Norwegian–Barents Sea continental margin. Geo Mar. Lett. 17 (2), 119–125.

Fine, I.V., Rabinovichb, A.B., Bornhold, B.D., Thomson, R.E., Kulikov, E.A., 2005. The Grand Banks landslide-generated tsunami of November 18, 1929: preliminary analysis and numerical modeling. Mar. Geol. 215, 45–57.

Frey-Martínez, J., Cartwright, J., James, D., 2006. Frontally confined versus frontally emergent submarine landslides: a 3D seismic characterisation. Mar. Petrol. Geol. 23 (5), 585–604.

Gee, M.J., Masson, D.G., Watts, A.B., Alleen, P.A., 1999. The Saharan debris fow: an insight into the mechanicsof long runout submarine debris flows. Sedimentology 46, 317–335.

Gue, C.S., 2012. Submarine Landslide Flows Simulation through Centrifuge Modelling. University of Cambridge. PhD Thesis.

Haflidason, H., Lien, R., Sejrup, H.P., Forsberg, C.F., Bryn, P., 2005. The Dating and Morphometry of the Storegga Slide. Ormen Lange–An Integrated Study for Safe Field Development in the Storegga Submarine Area. Elsevier.

Haflidason, H., Sejrup, H.P., Nygård, A., Mienert, J., Bryn, P., Lien, R., et al., 2004. The Storegga Slide: architecture, geometry and slide development. Mar. Geol. 213 (1–4), 201–234.

Hance, J.J., 2003. Development of a Database and Assessment of Seafloor Slope Stability Based on Published Literature. PhD Thesis. University of Texas at Austin.

Iverson, R.M., George, D.L., 2019. Basal stress equations for granular debris masses on smooth or discretized slopes. J. Geophys. Res.-Earth Surf. 124 (6), 1464–1484.

Kopf, A.J., Stegmann, S., Garziglia, S., Henry, P., Dennielou, B., Haas, S., et al., 2016. Soft sediment deformation in the shallow submarine slope off Nice (France) as a result of a variably charged Pliocene aquifer and mass wasting processes. Sediment. Geol. 344, 290–309.

Krastel, S., Schmincke, H.U., Jacobs, C.L., Rihm, R., Le Bas, T.P., Alibes, B., 2001. Submarine landslides around the canary islands. J. Geophys. Res. Solid Earth 106 (B3), 3977–3997.

Kvalstad, T.J., Andresen, L., Forsberg, C.F., Berg, K., Bryn, P., Wangen, M., 2005. The Storegga slide: evaluation of triggering sources and slide mechanics. Ormen Lange–an Integrated Study for Safe Field Development in the Storegga Submarine Area.

Laberg, J., Vorren, T., 1995. Late Weichselian submarine debris flow deposits on the Bear Island Trough mouth fan. Mar. Geol. 127 (1–4), 45–72.

Leshchinsky, B., Olsen, M.J., Mohney, C., O'Banion, M., Bunn, M., Allan, J., et al., 2019. Quantifying the sensitivity of progressive landslide movements to failure geometry, undercutting processes and hydrological changes. J. Geophys. Res.-Earth Surf. 124 (2), 616–638.

L'Heureux, J.S., Longva, O., Steiner, A., et al., 2012. Identification of weak layers and their role for the stability of slopes at Finneidfjord, Northern Norway. Submarine Mass Movements and Their Consequence 5st International Symposium 321–330.

Liu, J., Tian, J., Yi, P., 2015. Impact forces of submarine landslides on offshore pipelines. Ocean Eng. 95, 116–127.

Locat, A., Jostad, H.P., Leroueil, S., 2013. Numerical modeling of progressive failure and its implications for spreads in sensitive clays. Can. Geotech. J. 50 (9), 961–978.

Locat, A., Leroueil, S., Bernander, S., Demers, D., Jostad, H.P., Ouehb, L., 2011. Progressive failures in eastern Canadian and Scandinavian sensitive clays. Can. Geotech. J. 48 (11), 1696–1712.

Locat, A., Leroueil, S., Fortin, A., Demers, D., Jostad, H.P., 2015. The 1994 landslide at Sainte-Monique, Quebec: geotechnical investigation and application of progressive failure analysis. Can. Geotech. J. 52 (4), 490–504.

Longva, O., Janbu, N., Blikra, L.H., Boe, R., 2003. The 1996 Finneidfjord slide; seafloor failure and slide dynamics. In: Submarine Mass Movements and Their Consequences 1st International Symposium, pp. 531–538.

Løvholt, F., Pedersen, G., Harbitz, C.B., Glimsdal, S., Kim, J., 2015. On the characteristics of landslide tsunamis. Phil. Trans. Math. Phys. Eng. Sci. 373 (2053), 20140376.

Madrussani, G., Rossi, G., Rebesco, M., Picotti, S., Urgeles, R., Llopart, J., 2018. Sediment properties in submarine mass-transport deposits using seismic and rock-physics off NW Barents Sea. Mar. Geol. 402, 264–278.

Marr, J.G., Elverhøi, A., Harbitz, C., Imran, J., Harff, P., 2002. Numerical simulation of mud-rich subaqueous debris flows on the glacially active margins of the Svalbard–Barents Sea. Mar. Geol. 188 (3–4), 351–364.

Martorelli, E., Bosman, A., Casalbore, D., Falcini, F., 2016. Interaction of down-slope and along-slope processes off Capo Vaticano (southern Tyrrhenian Sea, Italy), with particular reference to contourite-related landslides. Mar. Geol. 378, 43–55.

Masson, D., Harbitz, C., Wynn, R., Pedersen, G., Løvholt, F., 2006. Submarine landslides: processes, triggers and hazard prediction. Phil. Trans. Math. Phys. Eng. Sci. 364 (1845), 2009–2039.

Migeon, S., Cattaneo, A., Hassoun, V., Dano, A., Casedevant, A., Ruellan, E., 2012. Failure Processes and Gravity-Flow Transformation Revealed by High-Resolution AUV Swath Bathymetry on the Nice Continental Slope (Ligurian Sea). Submarine Mass Movements and Their Consequences.

Moernaut, J., Wiemer, G., Reusch, A., Stark, N., De Batist, M., Urrutia, R., et al., 2017. The influence of overpressure and focused fluid flow on subaquatic slope stability in a formerly glaciated basin: Lake Villarrica (South-Central Chile). Mar. Geol. 383, 35–54.

Mohrig, D., Ellis, C., Parker, G., Whipple, K.X., Hondzo, M., 1998. Hydroplaning of subaqueous debris flows. Geol. Soc. Am. Bull. 110 (3), 387–394.

Moore, J.G., Clague, D.A., Holcomb, R.T., Lipman, P.W., Normark, W.R., Torresan, M.E., 1989. Prodigious submarine landslides on the Hawaiian Ridge. J. Geophys. Res. -Solid Earth. 94 (B12), 17465–17484.

Piper, D.J., Cochonat, P., Morrison, M.L., 1999. The sequence of events around the epicentre of the 1929 Grand Banks earthquake: initiation of debris flows and turbidity current inferred from sidescan sonar. Sedimentology 46 (1), 79–97.

Puzrin, A.M., Germanovich, L., Friedli, B., 2015a. Shear band propagation analysis of submarine slope stability. Geotechnique 66 (3), 188–201.

Puzrin, A.M., Germanovich, L., Kim, S., 2004. Catastrophic failure of submerged slopes in normally consolidated sediments. Geotechnique 54 (10), 631–643.

Puzrin, A.M., Gray, T., Hill, A., 2017. Retrogressive shear band propagation and spreading failure criteria for submarine landslides. Geotechnique 67 (2), 95–105.

Puzrin, A.M., Gray, T.E., Hill, A.J., 2015b. Significance of the actual nonlinear slope geometry for catastrophic failure in submarine landslides. Proc. R. Soc. A 471 (2175), 20140772.

Quinn, P.E., Diederichs, M.S., Rowe, R.K., Hutchinson, D.J., 2011. A new model for large landslides in sensitive clay using a fracture mechanics approach. Can. Geotech. J. 48, 1151–1162.

Quinn, P., Diederichs, M., Rowe, R., Hutchinson, D., 2012. Development of progressive failure in sensitive clay slopes. Can. Geotech. J. 49 (7), 782–795.

Randolph, M., Gourvenec, S., 2011. Offshore Geotechnical Engineering. CRC press, p. 2011.

Randolph, M.F., White, D.J., 2012. Interaction forces between pipelines and submarine slides—a geotechnical viewpoint. Ocean Eng. 48, 32–37.

Ren, Z., Liu, H., Li, L., Wang, Y., Sun, Q., 2023. On the effects of rheological behavior on landslide motion and tsunami hazard for the Baiyun Slide in the South China Sea. Landslides 20, 1599–1616.

Ren, Z., Zhao, X., Liu, H., 2019. Numerical study of the landslide tsunami in the South China Sea using Herschel-Bulkley rheological theory. Phys. Fluids 31 (5), 056601.

Ren, Y., Yang, Q., Wang, Y., Zhao, W., 2019. Experimental study on the undrained shear strength of deep-sea soft soil using improved T-bar penetrometer. Mar. Georesour. Geotechnol. 1–10.

Rui, Y., Yin, M., 2019. An analytical solution for the run-out of submarine debris flows. Mar. Geodesy 42 (3), 246–262.
Satake, K., Smith, J.R., Shinozaki, K., 2002. Three-Dimensional Reconstruction and Tsunami Model of the Nuuanu and Wailau Giant Landslides, Hawaii. Hawaiian Volcanoes. Deep Underwater Perspectives Geophysical Monograph 128.
Stoecklin, A., Friedli, B., Puzrin, A.M., 2017. Sedimentation as a control for large submarine landslides: mechanical modeling and analysis of the Santa Barbara Basin. J. Geophys. Res. Solid Earth 122 (11), 8645–8663.
Sultan, N., Savoye, B., Jouet, G., Leynaud, D., Cochonat, P., Henry, P., et al., 2010. Investigation of a possible submarine landslide at the Var delta front (Nice continental slope, southeast France). Can. Geotech. J. 47 (4), 486–496.
Sun, Q., Wang, Q., Shi, F., Alves, T., Gao, S., Xie, X., et al., 2022. Runup of landslide-generated tsunamis controlled by paleogeography and sea-level change. Communications Earth & Environment 3 (1), 244.
Talling, P.J., 2014. On the triggers, resulting flow types and frequencies of subaqueous sediment density flows in different settings. Mar. Geol. 352, 155–182.
Wang, C., Hawlader, B., 2017. Numerical modeling of three types of sensitive clay slope failures. In: Proceedings of the 19th International Conference on Soil Mechanics and Geotechnical Engineering. ICSMGE.
Wang, C., Hawlader, B., Islam, N., Soga, K., 2019. Implementation of a large deformation finite element modelling technique for seismic slope stability analyses. Soil Dynam. Earthq. Eng. 127, 105824.
Watt, S.F., Karstens, J., Micallef, A., et al., 2019. From catastrophic collapse to multi-phase deposition: Flow transformation, seafloor interaction and triggered eruption following a volcanic-island landslide. Earth Planet. Sci. Lett. 517, 135–147, 2019.
Watt, S.F.L., Talling, P.J., Vardy, M.E., Masson, D.G., Henstock, T.J., Hühnerbach, V., 2012. Widespread and progressive seafloor-sediment failure following volcanic debris avalanche emplacement: landslide dynamics and timing offshore Montserrat, Lesser Antilles. Mar. Geol. 323–325, 69–94 etal.
Whipple, K.X., 1997. Open-channel flow of Bingham fluids: applications in debris-flow research. J. Geol. 105 (2), 243–262.
Wilson, C.K, Long, D., Bulat, J., 2004. The morphology, setting and process of the Afen Slide. Mar. Geol. 213, 149–167, 2004.
Yin, M., Rui, Y., 2018. Laboratory study on submarine debris flow. Mar. Georesour. Geotechnol. 36 (8), 950–958.
Zhang, W., Klein, B., Randolph, M.F., Puzrin, A.M., 2021. Upslope failure mechanisms and criteria in submarine landslides: shear band propagation, slab failure and retrogression. J. Geophys. Res. Solid Earth 126 (9), e2021JB022041.
Zhang, W., Randolph, M.F., 2020. A smoothed particle hydrodynamics modelling of soil–water mixing and resulting changes in average strength. Int. J. Numer. Anal. Methods GeoMech. 44 (1–2), 1–22.
Zhang, W., Wang, D., Randolph, M.F., Puzrin, A.M., 2015. Catastrophic failure in planar landslides with a fully softened weak zone. Geotechnique 65 (9), 755–769.
Zhang, W., Wang, D., Randolph, M.F., Puzrin, A.M., 2016. Dynamic propagation criteria for catastrophic failure in planar landslides. Int. J. Numer. Anal. Methods GeoMech. 40 (17), 2312–2338.
Zhang, W., Wang, D., Randolph, M.F., Puzrin, A.M., 2017. From progressive to catastrophic failure in submarine landslides with curvilinear slope geometries. Geotechnique 67 (12), 1104–1119.
Zhang, X., Wang, L., Krabbenhoft, K., Tinti, S., 2019. A case study and implication: particle finite element modelling of the 2010 Saint-Jude sensitive clay landslide. Landslides 17 (10), 1–11.